Absolute Equation-of-State Measurement for Polystyrene from 25 – 60 Mbar Using a Spherically Converging Shock Wave

T. Döppner,[1] D. C. Swift,[1] A. L. Kritcher,[1] B. Bachmann,[1] G. W. Collins,[1] D. A. Chapman,[2] J. Hawreliak,[1] D. Kraus,[3,4] J. Nilsen,[1] S. Rothman,[2] L. X. Benedict,[1] E. Dewald,[1] D. E. Fratanduono,[1] J. A. Gaffney,[1] S. H. Glenzer,[5] S. Hamel,[1] O. L. Landen,[1] H. J. Lee,[5] S. LePape,[1] T. Ma,[1] M. J. MacDonald,[3] A. MacPhee,[1] D. Milathianaki,[5] M. Millot,[1] P. Neumayer,[6] P. A. Sterne,[1] R. Tommasini,[1] R. W. Falcone[3]

[1] *Lawrence Livermore National Laboratory, Livermore, California 94550, USA.*
[2] *AWE plc, Aldermaston, RG7 4PR, United Kingdom.*
[3] *University of California, Berkeley, California 94720, USA.*
[4] *Helmholtz-Zentrum Dresden-Rossendorf, 01328 Dresden, Germany.*
[5] *SLAC National Accelerator Laboratory, Menlo Park, California 94025, USA. and*
[6] *GSI Helmholtz-Zentrum für Schwerionenforschung, 64291 Darmstadt, Germany.*

We have developed an experimental platform for the National Ignition Facility (NIF) that uses spherically converging shock waves for absolute equation of state (EOS) measurements along the principal Hugoniot. In this Letter we present radiographic compression measurements for polystyrene that were taken at shock pressures reaching 60 Mbar (6 TPa). This significantly exceeds previously published results obtained on the Nova laser [Cauble et al., Phys. Rev. Lett. **80**, 1248 (1998)] at strongly improved precision, allowing to discriminate between different EOS models. We find excellent agreement with Kohn-Sham Density Functional Theory based molecular dynamics simulations.

PACS numbers: 62.50.-p,64.30.-t,52.77.Fv,52.35.Tc

Measuring the response of matter to extreme pressures that approach and exceed 100 Mbar (=10 TPa) is important for our understanding of giant planets [1, 2], brown dwarfs [3], large planetary impacts [4], and in laboratory inertial confinement fusion (ICF) plasmas [5, 6]. With the advent of high-power lasers such high-energy-density conditions can be created in a laboratory setting. We used the National Ignition Facility (NIF) [7] to drive a spherically converging shock wave and measured the equation of state (EOS) of polystyrene along the principal shock Hugoniot - describing the locus of thermodynamic final states accessible via shock compression from a given initial state - for pressures up to 60 Mbar.

Shock compression is the canonical technique to measure the EOS of matter at elevated pressure. Given a steady shock wave, conservation of mass, momentum, and energy across the shock discontinuity lead to the Rankine-Hugoniot relations [8]. It follows that the measurement of any two independent mechanical properties uniquely characterizes the shocked state. Such measurements can test and calibrate mechanical EOS-models, here in the sense of relations between mass density, internal energy, and pressure. High-precision EOS measurements based on optical velocimetry, tracking the shock velocity when transiting from a reference material into the sample under study, have been demonstrated [9]. While this impedance matching (IM) method [10, 11] is widely used, it relies on an accurate knowledge of the reference material [12]. Extending IM to higher pressures (more than ≈10 Mbar) is challenging because (1) reference materials are less well characterized and (2) the reflectivity at the shock front eventually degrades as material ahead of the shock front becomes ionized due to radiation from the shock–heated material, limiting the applicability of IM to transit time measurements. An alternative approach is measuring shock velocity and compression of the shocked state through radiography, which represents an absolute mechanical EOS measurement. This was demonstrated for polystyrene using planar shock waves by Cauble *et al.* for pressures up to 40 Mbar [13], although the accuracy in their measurements was not good enough to discriminate between todays state-of-the-art EOS models. More recently, spherically converging shock waves in solid spheres have found interesting applications [14–17] because they can act as pressure amplifiers - the shock pressure p increases roughly inversely with radius r ($p \propto 1/r$) [18] - up into the Gbar range, and they are stable against high-mode perturbations [19].

Here we present the first radiographic EOS measurements of a spherically converging shock wave in the laboratory. A polystyrene sample was used because a large body of experimental and theoretical work existed [9, 13, 20–24], high quality spherical targets were readily available, and experimental requirements could be met by existing NIF target platforms. Our experiments significantly advance the accuracy of high-pressure Hugoniot measurements and extend the data set up to 60 Mbar. The convergent geometry allows us to measure a range of locus points along the Hugoniot in one experiment. Here we present measurements of the principal Hugoniot for polystyrene at pressures from 25 to 60 Mbar, cf. Fig. 1. We adapt the indirect drive concept to drive a spherical shock into a solid plastic sphere, illustrated

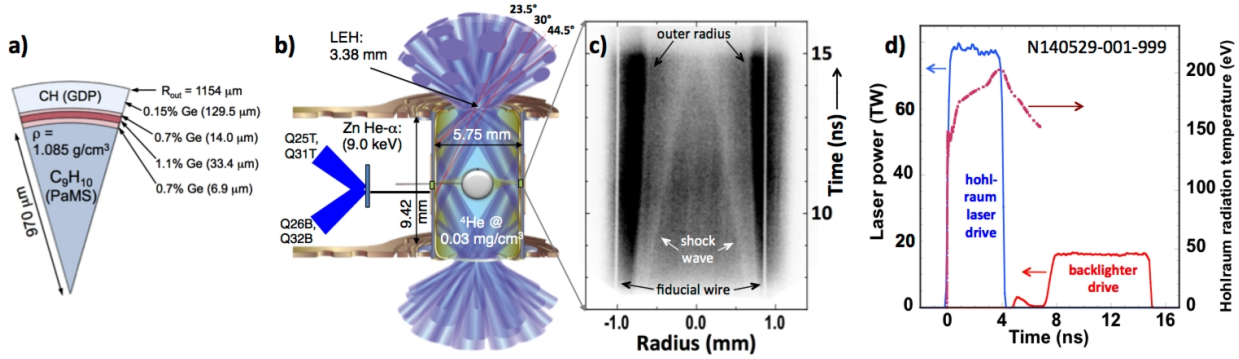

FIG. 1: The 1D radiography convergent ablator platform [31] (b) is used to measure time-resolved (streaked) radial transmission profiles ((c) shows the raw streak image) of a converging shock wave in a solid plastic sphere of initially 2.3 mm diameter. (a) shows the dimensions and composition of the spherical plastic sphere used in this experiment, and the thicknesses of the Ge-doped layers, where doping levels are given in atomic number %. The temporal laser profiles driving the hohlraum and the backlighter foil are shown in (d) along with the measured hohlraum radiation temperature.

in Fig. 1b. We use a cylindrical gold cavity (hohlraum) with an inner diameter of 5.75 mm, a height of 9.42 mm, and laser entrance holes (LEHs) of 3.38 mm diameter. 168 laser beams enter the hohlraum through the LEHs, and generate a symmetric soft x-ray drive by heating the inner hohlraum wall. The plastic sphere is mounted at the center of the hohlraum, which is supported by 45.6-nm-thin plastic membranes. The main sample material, a 1940 μm diameter poly(α-methylstyrene) (PaMS, C_9H_{10}) sphere, is overcoated with a 183.8 μm thick plastic ablator (GDP: glow-discharge polymer) that contains a graded Ge dopant layer close to the interface with the PaMS sample, see Fig. 1a for detailed thickness and dopant levels. The Ge doping serves two purposes: (i) it acts as a pre-heat shield by attenuating non-thermal Au M-band x-rays (2.5–3.5 keV) from the Au hohlraum wall, and (ii) it provides a fiducial for the enclosed sample mass, which can be used as an additional constraint for the radiographic analysis [25, 26]. The Hugoniot measurement starts when the shock wave enters the PaMS sample. For the remainder of this Letter we use polystyrene to refer to PaMS in our experiment.

Heating of the sample prior to shock arrival can limit its compressibility [17]. There are several mechanisms that could cause pre-heating: (1) gold M-band emission from the hohlraum wall, (2) hot electrons generated through laser-plasma-interaction instabilities (LPI) or (3) thermal emission from the shock front. To rule out hot electron pre-heat, we used a near vacuum hohlraum drive that has demonstrated a low level of hot electron generation [27] due to LPI instabilities being almost absent. For this purpose the target was fielded at room temperature (293 K) with a low density ^{4}He hohlraum gas fill of 0.03 mg/cm^3 (p = 0.195 bar). To minimize other pre-heat sources, we chose a low-energy drive where 168 laser beams delivered a total of 311 kJ at a wavelength of 351 nm and peak laser power of 78.0 TW into the hohlraum in a 4 ns-long, nearly square drive pulse (Fig. 1d). The peak hohlraum radiation temperature was measured at (203 $\pm$ 3) eV at the end of the hohlraum drive by the DANTE diagnostic [28, 29] with an Au M-band fraction of only 5% [30]. Hydrodynamics simulations matching these drive observables predict pre-heat due to M-band emission to be less than 0.3 eV. This low pre-heat level does not impact the compressibility of the sample and therefore the Hugoniot measurement in the pressure range reported here [17].

To track the shock velocity and the compression at the shock front we use a streaked x-ray radiography platform that was originally developed for ICF capsule implosion velocity measurements [31, 32]. Here, the 100-μm-high, horizontal slice of the solid sample at the center of the hohlraum is backlit with a Zn He-α (9.0 keV) area backlighter. The 15-μm-thick Zn backlighter foil is driven using four NIF quads, 16 laser beams, with a total of 123 kJ over 7 ns as shown in Fig. 1d. The backlighter laser pulse has a pre-pulse to precondition the plasma and increase the conversion efficiency during the main pulse [33]. A 16 μm wide imaging slit was placed at 103.0 $\pm$ 0.3 mm from the sample. The one-dimensional image enters the entrance slit of the streak camera cathode, which is located 783 mm downstream of the imaging slit. The spatial resolution for this setup is 18 μm. The entrance slit of the streak camera has a height of 500 μm. Given the streak duration (9.6 ns), internal magnification and detector dimension the integration time of a given state is 155 ps. Fig. 1c shows the raw data of the resulting radiograph. The trajectory of the shock wave, which leads to reduced transmission, can clearly be seen. The spherical shock accelerates and converges at the center of the sphere near the end of the streaked data. Also clearly visible is the outer edge of the sphere, which has a radius of 720 μm at maximum sample compression. Just inside of the outer radius the Ge-doped layer is located, which

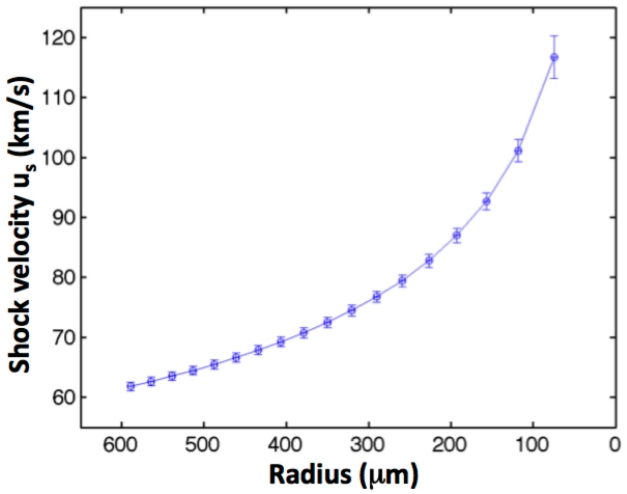

FIG. 2: Measured shock velocity of a converging shock wave in a solid polystyrene sphere, which exceeds 100 km/s near the center of the sphere.

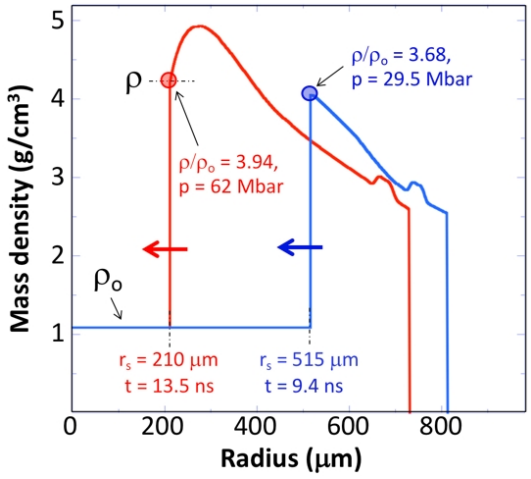

FIG. 3: Inferred radial mass density profiles at two different times as the shock moves inwards. Inside the shock is the pristine polystyrene sample at solid density of $\rho_0 = 1.085$ g/cm^3.

contributes to the sharp appearance of the outer edge and which can be traced throughout the implosion. Outside the compressed capsule region, the shadows of two alignment fiducial wires can be seen, which are placed in front of the cathode. We use them to de-warp the data image and extract the internal magnification of the streak camera, yielding the total magnification of the imaging system of $M = 9.21 \pm 0.07$. From the streaked radiograph, the trajectory and the resulting shock velocity, u_s, can be directly extracted. Fig. 2 shows u_s as function of radius, highlighting the acceleration due to convergence to more than 100 km/s at small radii. Since the thickness of the shock front is on order of the mean free ion path [34], which is $\ll 1\,\mu$m for conditions encountered in this experiment, the shock can locally be considered steady as in the well-established planar case. Therefore, u_s can be related to pressure p by the Rankine-Hugoniot relations [8] through

$$p = p_0 + u_s^2 \rho_0 \left(1 - \frac{\rho_0}{\rho}\right) \qquad (1)$$

if the mass density ρ at the shock front is known. Here p_0 is ambient pressure, and $\rho_0 = 1.085 \pm 0.005$ g/cm^3 is the initial polystyrene mass density.

States along the shock Hugoniot were deduced by reconstructing the density distribution $\rho(r,t)$, locating the locus of the shock front $r_s(t)$ and hence the shock compression $\rho(r_s(t),t)/\rho_0$. The shock speed $u_s(t)$ is obtained by differentiating $r_s(t)$, giving a locus of states along the Hugoniot, $\rho(u_s)$. The density distribution was reconstructed by profile-matching rather than Abel inversion, as this allowed us to use the un-shocked region as a strong constraint on the shock compression, and is a more natural framework for compensating for low signal levels by smoothing over time and radius [26, 35]. Fig. 3 shows two examples of inferred mass density profiles. One can clearly see material piling up behind the shock front as time progresses as a typical feature for a converging shock wave [25]. $\rho(r_s)$ is the density at the shock front, as illustrated in Fig. 3, and represents a fit parameter in the radial density profile function. The increased density feature near the outer edge is due to the Ge-doped layer (cf. Fig. 1a), and is used to constrain the enclosed mass in the radiographic analysis. The corresponding measured and fitted sample transmission profiles are shown in Fig. 4.

The sensitivity to the choice of density profile functions was studied, in particular by fitting the entire time-radius-density distribution, compared with fitting shorter slices in time for which the density variation could be

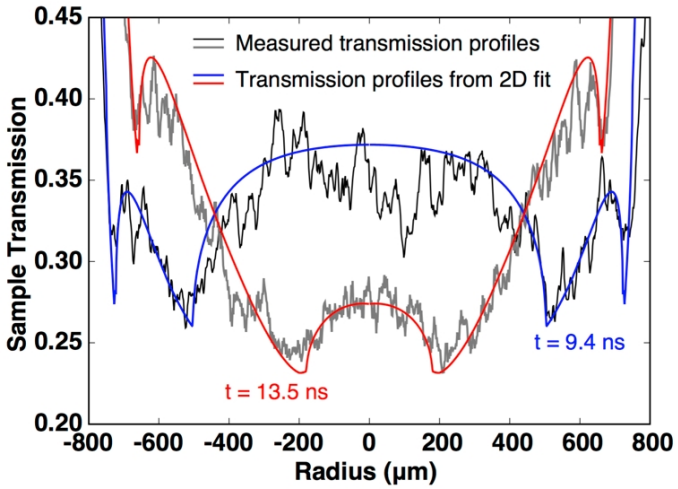

FIG. 4: Comparison of the measured and inferred sample transmission profiles that correspond to the inferred mass density profiles shown in Fig. 3.

represented with simpler functions and fewer parameters. The spatial brightness profile of the x-ray backlighter was included as additional parameters for optimization.

Our analysis accounts for the blurring of the shock front due to its curvature. In order to avoid large blurring near the center of the sphere, we restrict the analysis to shock radii larger than 200 μm, which corresponds to a shock pressure of ∼60 Mbar. At these pressures and below, for which simulations predict temperatures to not exceed 35 eV, ionization of the carbon K-shell electrons can safely be ruled out, justifying the assumption of cold opacities for our analysis. Consistent results were obtained with a fit to the entire ($r > 200\,\mu$m) convergence history of the radiograph, from which compression and pressure along the Hugoniot are inferred. Fig. 5 shows the results of this analysis and compares it with previously reported Hugoniot measurements [9, 13, 20], the Sesame EOS table 7592 [36] and DFT simulations [22]. Our NIF results are shown as a probability distribution with contours of the statistical error ($1\sigma \approx 3.7\%$) for the compression. The statistical error represents the uncertainty inferred from fitting the time-space density profile to match the streaked radiography image [26]. The systematic error for the compression of 1.0% is dominated by the uncertainty in spatial scale and background subtraction. Since shock velocity can be measured to high accuracy ($\delta u_s/u_s = \pm 1.1\%$) by smoothing along the trajectory, the uncertainty in compression dominates the uncertainty in shock pressure ($\delta p/p = \pm 6.9\%$) per Eq. (1). Fig. 5a shows a representative single Hugoniot data point with total error bars. We note that all previous work was done with C_1H_1, i.e. at a slightly different stoichiometry. The data sets of Ozaki *et al.* [20] and Barrios *et al.* [9] were re-analyzed using the latest EOS of the quartz impedance matching standard [12]. We also note that samples with a more complicated phase diagram (such as containing phase changes) might require more thorough analysis.

Our new experimental measurements between 25 and 60 Mbar are in very good agreement with the Hugoniot curve extracted from Kohn-Sham Density Functional Theory (KS-DFT) molecular dynamics simulations, which use pseudo-potentials to treat the 1s electrons in carbon [22]. Our data indicate slightly lower compressibility than predicted by the Sesame EOS table 7592 [36]. With increasing pressures details of the electronic structure are expected to affect the shape of the Hugoniot curve. The Sesame EOS table does not show this level of detail as it is derived from the Thomas-Fermi-Dirac model [36–38], which neglects the effects of electronic shell structure in atoms. A more nuanced description of electronic excitations including atomic shell structure is possible with KS-DFT. To compare directly with the average-atom Thomas-Fermi based Sesame-7592, we employ an EOS model for carbon [39] based on the average-atom KS-DFT approach, Purgatorio [40, 41]. We then use an equal-(P,T), additive-volume mixing scheme [42] to produce a C_9H_{10} EOS by combining this carbon EOS with the hydrogen EOS of Ref. [43]. The Hugoniot curve for the resulting EOS is shown in Fig. 5 labeled as *mix-PC*. Substituting the hydrogen EOS of Ref. [43] for the very different model of Ref. [44] does little to affect the Hugoniot of C_9H_{10} above ∼100 Mbar.

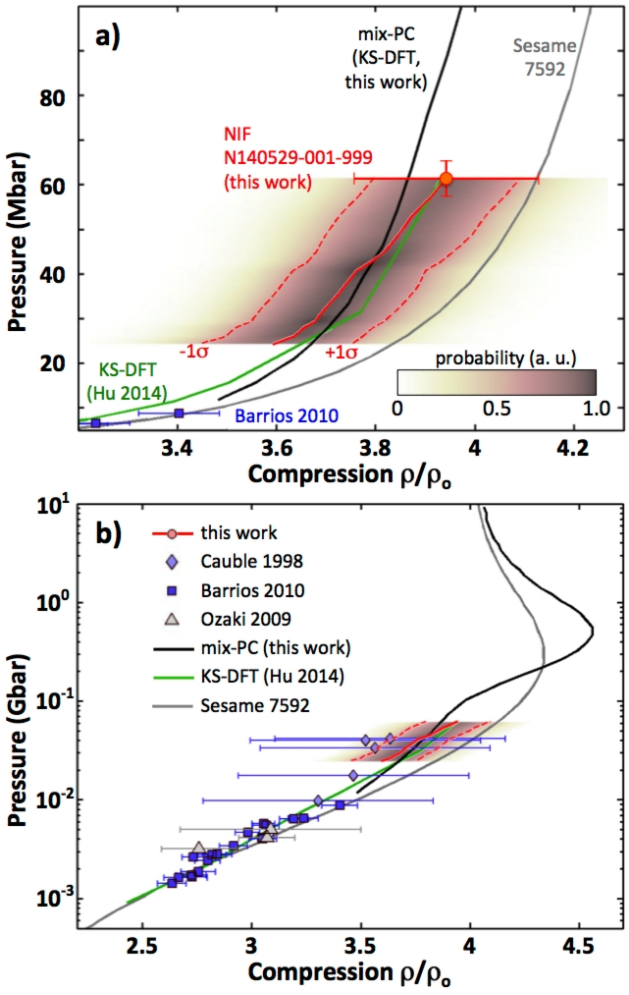

FIG. 5: Principal Hugoniot measurement of polystyrene (PaMS: C_9H_{10}) at the NIF (experiment N140529-001-999). 1σ contours of the *statistical* error are shown. Additionally, the top panel (a) shows one representative NIF data point with *total* error bars. The lower panel (b) sets the new data into context with previous results from planar shock experiments [9, 13, 20], the Sesame 7592 EOS table [36] and Kohn-Sham DFT simulations [22].

The mix-PC curve in Fig. 5b shows an inflection just above 100 Mbar, which coincides approximately with the beginning of the K-shell ionization in carbon, leading to higher heat capacity and increased compressibility. Recent experimental observations show evidence for larger-than-expected ionization potential depression in dense plasmas and have challenged the applicability of commonly used ionization models in high energy den-

sity plasmas [45–47]. Future experiments using convergent shocks at higher pressures will probe this interesting physics regime, which will require further improvements in the analysis techniques. These experiments will provide an alternative approach for measuring ionization potential depression. Pressures of several 100 Mbar can be achieved by increasing the hohlraum radiation temperature from 200 to 300 eV (∼4x increase in ablation pressure) and extending the radiography measurement to radii as small as 100 μm (2x pressure increase).

In summary, we have successfully measured the principal shock Hugoniot of polystyrene in the pressure range of 25 to 60 Mbar using radiography of a spherically converging shock wave, generated by a symmetric hohlraum drive at the National Ignition Facility. The converging shock samples a range of pressures in a single experiment, rising to several times the ablation pressure of 20 Mbar applied to the outside of the sample. Our Hugoniot data are in good agreement with KS-DFT based modeling, while the measured curve is slightly stiffer than predicted using the SESAME table 7592. We have demonstrated an experimental capability for absolute EOS measurements in low–Z elements for pressures $\gg$ 10 Mbar. This technique also provides a path towards developing EOS standards at such pressures that can then be used for impedance matching measurements for mid- and high-Z elements.

We would like to thank the entire NIF operations, cryogenics, diagnostics, and target teams for outstanding support. We would like to thank L. Divol, L. Berzak Hopkins, M. Patel and O. Jones for discussions on the hohlraum drive, R. Redmer and R. Bredow for providing and discussing Hugoniot calculations, P. Celliers for many valuable discussions, and J. Fry and S. Felker for support in target design and production. This work was performed under the auspices of the U.S. Department of Energy by Lawrence Livermore National Laboratory under Contract No. DE-AC52-07NA27344. The authors acknowledge support from Laboratory Directed Research and Development Grant No. 13-ERD-073. R.W.F. and D.K. acknowledge support from SSAA program Contract No. DE-FG52-06NA26212. S.H.G acknowledges support for HED science at SLAC through DOE FES under FEP 100182.

[1] D. C. Swift, J. H. Eggert, D. G. Hicks, S. Hamel, K. Caspersen, E. Schwegler, G. W. Collins, N. Nettelmann, and G. J. Ackland, Astrophys. J. **744**, 59 (2012).
[2] L. Stixrude, Phys. Rev. Lett. **108**, 055505 (2012).
[3] T. Nakajima, B. R. Oppenheimer, S. R. Kulkarni, D. A. Golimowski, K. Matthews, and S. T. Durrance, Nature **378**, 463 (1995).
[4] P. Schulte, L. Alegret, I. Arenillas, J. A. Arz, P. J. Barton, P. R. Bown, T. J. Bralower, G. L. Christeson, P. Claeys, C. S. Cockell *et al.*, Science **327**, 1214 (2010).
[5] J. D. Lindl, P. Amendt, R. L. Berger, S. G. Glendinning, S. H. Glenzer, S. W. Haan, R. L. Kauffman, O. L. Landen, and L. J. Suter, Phys. Plasmas **11**, 339 (2004).
[6] O. A. Hurricane, D. A. Callahan, D. T. Casey, P. M. Celliers, C. Cerjan, E. L. Dewald, T. R. Dittrich, T. Döppner, D. E. Hinkel, L. F. Berzak Hopkins *et al.*, Nature **506**, 343 (2014).
[7] E. I. Moses, G. H. Miller, and C. R. Wuest, Nucl. Fusion **44**, 228 (2004).
[8] Y. Zeldovich and Y. Raizer, Physics of Shock Waves and High-Temperature Hydrodynamic Phenomena, Dover Books on Physics, Mineola NY (2002).
[9] M. A. Barrios, D. G. Hicks, T. R. Boehly, D. E. Fratanduono, J. H. Eggert, P. M. Celliers, G. W. Collins, and D. D. Meyerhofer, Phys. Plasmas **17**, 056307 (2010).
[10] A. C. Mitchell and W. J. Nellis, J. Appl. Phys. **52**, 3363 (1981).
[11] P. M. Celliers, G. W. Collins, D. G. Hicks, and J. H. Eggert, J. Appl. Phys. **98**, 113529 (2005).
[12] M. D. Knudson and M. P. Desjarlais, Phys. Rev. B **88**, 184107 (2013).
[13] R. Cauble, T. S. Perry, D. R. Bach, K. S. Budil, B. A. Hammel, G. W. Collins, D. M. Gold, J. Dunn, P. Celliers, and L. B. Da Silva *et al.*, Phys. Rev. Lett. **80**, 1248 (1998).
[14] R. Nora, W. Theobald, R. Betti, F. J. Marshall, D. T. Michel, W. Seka, B. Yaakobi, M. Lafon, C. Stoeckl, J. Delettrez *et al.*, Phys. Rev. Lett. **114**, 045001 (2015).
[15] W. Theobald, R. Nora, W. Seka, M. Lafon, K. S. Anderson, M. Hohenberger, F. J. Marshall, D. T. Michel, A. A. Solodov, C. Stoeckl *et al.*, Phys. Plasmas **22**, 056310 (2015).
[16] H. Sawada, S. Lee, T. Shiroto, H. Nagatomo, Y. Arikawa, H. Nishimura, T. Ueda, K. Shigemori, A. Sunahara, N. Ohnishi *et al.*, Appl. Phys. Lett. **108**, 254101 (2016).
[17] A. L. Kritcher, T. Döppner, D. Swift, J. Hawreliak, G. Collins, J. Nilsen, B. Bachmann, E. Dewald, D. Strozzi, S. Felker *et al.*, High Energ. Dens. Phys. **10**, 27 (2014).
[18] A. L. Kritcher, T. Döppner, D. Swift, J. Hawreliak, J. Nilsen, J. Hammer, B. Bachmann, G. Collins, C. Keane, S. Glenzer *et al.*, J. Phys.: Conf. Ser. **688**, 012055 (2016).
[19] M. Murakami, J. Sanz, and Y. Iwamoto, Phys. Plasmas **22**, 072703 (2015).
[20] N. Ozaki, T. Sano, M. Ikoma, K. Shigemori, T. Kimura, K. Miyanishi, T. Vinci, F. H. Ree, H. Azechi, T. Endo *et al.*, Phys. Plasmas **16**, 062702 (2009).
[21] H. Shu, X. Huang, J. Ye, J. Wu, G. Jia, Z. Fang, Z. Xie, H. Zhou, and S. Fu, Eur. Phys. J. D **69**, 259 (2015).
[22] S. X. Hu, T. R. Boehly, and L. A. Collins, Phys. Rev. E **89**, 063104 (2014).
[23] S. X. Hu, L. A. Collins, V. N. Goncharov, J. D. Kress, R. L. McCrory, and S. Skupsky, Phys. Rev. E **92**, 043104 (2015).
[24] S. Zhang, K. P. Driver, F. Soubiran, and B. Militzer, Phys. Rev. E **96**, 013204 (2017).
[25] D. Swift, J. Hawreliak, D. Braun, A. Kritcher, S. Glenzer, G. W. Collins, S. Rothman, D. Chapman, S. Rose, and M. L. Elert, AIP Conf. Proc. **1426**, 477 (2012).
[26] D. C. Swift *et al.*, submitted
[27] S. Le Pape, L. Divol, L. Berzak Hopkins, A. Mackinnon, N. B. Meezan, D. Casey, J. Frenje, H. Herrmann,

J. McNaney, T. Ma *et al.*, Phys. Rev. Lett. **112**, 225002 (2014).
[28] E. L. Dewald, K. M. Campbell, R. E. Turner, J. P. Holder, O. L. Landen, S. H. Glenzer, R. L. Kauffman, L. J. Suter, M. Landon, M. Rhodes,and D. Lee, Rev. Scient. Instrum. **75**, 3759 (2004).
[29] N. B. Meezan, A. J. MacKinnon, D. G. Hicks, E. L. Dewald, R. Tommasini, S. Le Pape, T. Döppner, T. Ma, D. R. Farley, D. H. Kalantar *et al.*, Phys. Plasmas **20**, 056311 (2013).
[30] We define the Au M-band fraction as the ratio of spectral emission above 1.8 keV divided by the full spectrum.
[31] D. G. Hicks, N. B. Meezan, E. L. Dewald, A. J. MacKinnon, R. E. Olson, D. A. Callahan, T. Döppner, L. R. Benedetti, D. K. Bradley, P. M. Celliers *et al.*, Phys. Plasmas **19**, 122702 (2012).
[32] Y. P. Opachich, D. H. Kalantar, A. G. MacPhee, J. P. Holder, J. R. Kimbrough, P. M. Bell, D. K. Bradley, B. Hatch, G. Brienza-Larsen, C. Brown *et al.*, Rev. Scient. Instrum. **83**, 125105 (2012).
[33] M. A. Barrios, K. B. Fournier, S. P. Regan, O. Landen, M. May, Y. P. Opachich, K. Widmann, D. K. Bradley, and G. W. Collins, High Energ. Dens. Phys. **9**, 626 (2013).
[34] R.W. Fox and A.T. MacDonald, Introduction to Fluid Mechanics, Wiley, Hoboken NJ (1992).
[35] G. S. Cunningham, K. M. Hanson, G. R. Jennings, Jr, and D. R. Wolf, Rev. Progr. Quant. NDE **14A**, 747 (1995).
[36] J. Abdallah Jr., User's Manual for GRIZZLY, Los Alamos National Laboratories Report No. LA-10244-M (1984).
[37] L. H. Thomas, Mathematical Proceedings of the Cambridge Philosophical Society **23**, 542 (1927).
[38] E. Fermi, Rend. Accad. Naz. Lincei **6**, 32 (1927).
[39] L. X. Benedict, K. P. Driver, S. Hamel, B. Militzer, T. Qi, A. A. Correa, A. Saul, and E. Schwegler, Phys. Rev. B **89**, 224109 (2014).
[40] D. A. Liberman, Phys. Rev. B **20**, 4981 (1979).
[41] B. Wilson, V. Sonnad, P. Sterne, and W. Isaacs, J. Quant. Spectrosc. Ra. **99**, 658 (2006).
[42] S. Hamel, L. X. Benedict, P. M. Celliers, M. A. Barrios, T. R. Boehly, G. W. Collins, T. Döppner, J. H. Eggert, D. R. Farley, D. G. Hicks *et al.*, Phys. Rev. B **86**, 094113 (2012).
[43] G. I. Kerley, Sandia National Laboratories Technical Report SAND2003, 3613 (2003).
[44] D. A. Young, High Pressure Res. **16**, 389 (2000).
[45] O. Ciricosta, S. M. Vinko, H.-K. Chung, B.-I. Cho, C. R. D. Brown, T. Burian, J. Chalupský, K. Engelhorn, R. W. Falcone, C. Graves *et al.*, Phys. Rev. Lett. **109**, 065002 (2012).
[46] L. B. Fletcher, A. L. Kritcher, A. Pak, T. Ma, T. Döppner, C. Fortmann, L. Divol, O. S. Jones, O. L. Landen, H. A. Scott *et al.*, Phys. Rev. Lett. **112**, 145004 (2014).
[47] D. Kraus, D. A. Chapman, A. L. Kritcher, R. A. Baggott, B. Bachmann, G. W. Collins, S. H. Glenzer, J. A. Hawreliak, D. H. Kalantar, O. L. Landen *et al.*, Phys. Rev. E **94**, 011202 (2016).